

Article

Non-Adiabatic Excited-State Time-Dependent GW (TDGW) Molecular Dynamics Simulation of Nickel-Atom Aided Photolysis of Methane to Produce a Hydrogen Molecule

Aaditya Manjanath ¹, Ryoji Sahara ¹, Yoshiyuki Kawazoe ^{2,3,4} and Kaoru Ohno ^{1,5,*}

¹ Research Center for Structural Materials, National Institute for Materials Science (NIMS), 1-2-1 Sengen, Tsukuba 305-0047, Ibaraki, Japan; manjanath.aaditya@nims.go.jp (A.M.); sahara.ryoji@nims.go.jp (R.S.)

² New Industry Creation Hatchery Center, Tohoku University, 6-6-4 Aramaki Aza Aoba, Aoba-ku, Sendai 980-8579, Miyagi, Japan; kawazoe@e-workshop.co.jp

³ School of Physics, Institute of Science, Suranaree University of Technology, 111 University Avenue, Nakhon Ratchasima 30000, Thailand

⁴ Physics and Nanotechnology, SRM Institute of Science and Technology, Tamil Nadu, Kattankurathur 603203, India

⁵ Department of Physics, Graduate School of Engineering, Yokohama National University (YNU), 79-5 Tokiwadai, Hodogaya-ku, Yokohama 240-8501, Kanagawa, Japan

* Correspondence: ohno@ynu.ac.jp

Abstract: Methane photolysis is a very important initiation reaction from the perspective of hydrogen production for alternative energy applications. In our recent work, we demonstrated using our recently developed novel method, non-adiabatic excited-state time-dependent GW (TDGW) molecular dynamics (MD), how the decomposition reaction of methane into a methyl radical and a hydrogen atom was captured accurately via the time-tracing of all quasiparticle levels. However, this process requires a large amount of photoabsorption energy (PAE ~ 10.2 eV). Moreover, only one hydrogen atom is produced via a single photon absorption. Transition metal atoms can be used as agents for photochemical reactions, to reduce this optical gap and facilitate an easier pathway for hydrogen production. Here, we explore the photolysis of methane in the presence of a Ni atom by employing TDGW-MD. We show two possibilities for hydrogen-atom ejection with respect to the location of the Ni atom, towards the Ni side or away from it. We demonstrate that only the H ejection away from the Ni side facilitates the formation of a hydrogen molecule with the quasiparticle level corresponding to it having an energy close to the negative ionization potential of an isolated H₂ molecule. This is achieved at a PAE of 8.4 eV which is lower compared to that of pristine methane. The results obtained in this work are an encouraging step towards transition metal-mediated hydrogen production via photolysis of hydrocarbons.

Keywords: quasiparticle; Koopmans' theorem; TDDFT; GW approximation; Ni atom; CH₄; chemical reaction; photochemistry; surface hopping



Citation: Manjanath, A.; Sahara, R.; Kawazoe, Y.; Ohno, K. Non-Adiabatic Excited-State Time-Dependent GW (TDGW) Molecular Dynamics Simulation of Nickel-Atom Aided Photolysis of Methane to Produce a Hydrogen Molecule. *Nanomaterials* **2024**, *14*, 1775. <https://doi.org/10.3390/nano14221775>

Academic Editors: Luis Alberto Ruiz Pestana, Wenjie Xia and Zhaoxu Meng

Received: 30 September 2024

Revised: 30 October 2024

Accepted: 2 November 2024

Published: 5 November 2024



Copyright: © 2024 by the authors. Licensee MDPI, Basel, Switzerland. This article is an open access article distributed under the terms and conditions of the Creative Commons Attribution (CC BY) license (<https://creativecommons.org/licenses/by/4.0/>).

1. Introduction

Methane is a very important fuel gas as (a) it is a main constituent of liquefied natural gas (LNG) [1], which is useful for long-distance transport, (b) it is the main component of biofuel or biogas [2], making it a source of clean energy, and (c) it is useful as a direct coolant in jet engines. In addition, methane serves as a precursor gas for hydrogen production. H₂ is considered the “fuel of the future” because it produces three times the amount of energy (39.4 kWh kg⁻¹) compared to other fuels such as liquid hydrocarbons (13.1 kWh kg⁻¹) [3]. It has been reported extensively that the endothermic decomposition of methane leads to the production of hydrogen. Cracking [4] (heating of methane in the absence of air), photolysis [5–9] (photoexcitation of methane), and steam reforming [10,11] (reaction of methane with steam), as well as thermocatalytic decomposition [12–16] and solar-aided

decomposition [17–20], both of which produce hydrogen along with “carbon black” or nano-sized carbon clusters, without emitting greenhouse gases, are the most commonly employed processes for this.

From the perspective of hydrogen production, it is interesting and important to investigate the photochemical reactions of hydrocarbons. The computational approach is more favorable than the typical experimental approach when investigating ultrafast reactions such as photolysis. However, density functional theory (DFT) [21] is, in principle, a ground-state theory and cannot be applied to any photoexcited state. Time-dependent density functional theory (TDDFT) [22] relying on adiabatic local density approximation (ALDA) [23] has been the standard approach to investigate the excited-state (ES) dynamics; however, it faces a longstanding difficulty of ALDA not being applicable to the time-dependent (TD) molecular dynamics (MD) for an initially excited state (ES). We have recently overcome this difficulty [24] by employing extended quasiparticle theory (EQPT) [25,26], in which the full correspondence is achieved between the ES surfaces and corresponding total energies, with satisfying extended Koopmans’ theorem [27,28]. In EQPT, each quasiparticle (QP) level is related to a total energy difference. The QP energies of an occupied level ($\varepsilon_i^{\text{QP}}$) and an unoccupied level ($\varepsilon_a^{\text{QP}}$) are defined, respectively, as

$$\varepsilon_i^{\text{QP}} = E_{\text{ref}}^{(N)} - E_{i \rightarrow \text{vac}}^{(N-1)}, \quad (1a)$$

$$\varepsilon_a^{\text{QP}} = E_{\text{vac} \rightarrow a}^{(N+1)} - E_{\text{ref}}^{(N)}, \quad (1b)$$

where $E_{\text{ref}}^{(N)}$, $E_{i \rightarrow \text{vac}}^{(N-1)}$, and $E_{\text{vac} \rightarrow a}^{(N+1)}$ are the total energies of the reference N -electron system, the $(N - 1)$ -electron system formed by removing an electron from the i th occupied level to the vacuum level (vac), and the $(N + 1)$ -electron system formed by adding an electron at the a th unoccupied level from vac. Here, we emphasize that the reference N -electron system is not necessarily the ground state (GS), but can be any of the excited eigenstates. The QP energies $\varepsilon_i^{\text{QP}}$ and $\varepsilon_a^{\text{QP}}$ in Equation (1) can be referred to as ‘negative ionization potentials’ and ‘negative electron affinities’, respectively, and have a direct correspondence with the observations from photoemission/inverse photoemission experiments. The GW approximation (GWA) is in full conformity with EQPT. We have applied EQPT within the GWA to the mixed quantum-classical Ehrenfest dynamics with surface hopping (SH) and developed the NA-ES-TDGW (TDGW) MD method [24]. The merit of this method is that we can trace all the QP energies as well as the QP wavefunctions, which we will refer to as “charge densities”, during the simulation. Using this method, we have successfully investigated methane photolysis $\text{CH}_4 \xrightarrow{\hbar\omega} \text{CH}_3\cdot + \text{H}$ at the lowest photoexcited state [24], which is considered as the initiation reaction of a complex multi-step process of a variety of methane combustion and hydrogen production reactions.

Nevertheless, the photolysis of methane requires a large photoexcitation energy. In this regard, transition metal atoms can pave the way for reducing such large optical gaps and facilitate an easier pathway for hydrogen production. Here, we focus on the effect of a transition atom in this reaction. The aim of the present study is to unravel new reaction pathways in nickel atom-mediated methane photolysis. To the best of our knowledge, there has been no direct molecular dynamics study to search the reaction pathway of CH_4 in the presence of a transition metal atom at any of the photoexcited states, although there have been several computational studies involving systems with transition metal atoms. One such study is the TDDFT molecular dynamics investigation of the hydrogen spillover process via Ni dimers by Sahara et al. [29]. They showed that a hydrogen molecule can be dissociated into two hydrogen atoms near the Ni dimer by a small excitation energy. Another is a DFT study on the potential energy surfaces of a CH_4 molecule with a Ni atom by Burghgraef et al. [30] or with an Fe atom by Sun et al. [31]. From their results, reactions such as $\text{CH}_4 + \text{M} \longrightarrow \text{CH}_3\text{MH}$ ($\text{M} = \text{Ni}$ or Fe) can be expected. Concerning the late-stage dynamics of the thermocatalytic decomposition of methane, there is a DFT study on the potential energy surface of a Ni_{55} cluster with an open (semi-capped) carbon nanotube by

Wang et al. [32]. Although the earlier stage of methane decomposition was not considered in their work, the mechanism of the catalytic behavior of the Ni cluster was clarified.

The presence of a Ni atom breaks the tetrahedral symmetry of CH₄, rendering a non-unique choice of the photoexcited state. The highest occupied molecular orbital (HOMO) of this system is no more that of the methane fragment but is now one of the highest occupied Ni 3*d* levels. Moreover, the lowest unoccupied molecular orbital (LUMO) of this system is no more than the negative electron affinity level of pure CH₄ above the vacuum level but is the lowest unoccupied Ni 3*d* level, which is below the vacuum level. This means that there are several possible reaction pathways depending on the choice of the photoexcited excited state, for which the excitation energy is lower than 10.2 eV [5–7] that is needed in the photolysis of the pristine methane case. In the course of our study, we show that there are at least two possible pathways of methane decomposition. In one case, hydrogen atoms on the side opposite Ni are ejected from the methane molecule, while in the other case, hydrogen atoms facing the Ni atom are ejected from the methane molecule. We present the results of the two different pathways in detail in Section 3.

2. Method

2.1. Time-Dependent QP Equation

The wavepackets $\phi_\lambda(\mathbf{r}; \mathbf{R}(t), t)$, where $\mathbf{r}, \mathbf{R}(t) = \{\mathbf{R}_I(t)\}$, and t represent the position of the QP, a set of nuclear coordinates (I - atomic index), and time, respectively, satisfy the time-dependent QP (TDQP) equation [24]

$$i \frac{\partial}{\partial t} \phi_\lambda(\mathbf{r}; \mathbf{R}(t), t) = \mathcal{H}_{\text{mixed}}^{\text{QP}}(\mathbf{r}; \mathbf{R}(t)) \phi_\lambda(\mathbf{r}; \mathbf{R}(t), t), \quad (2)$$

which is similar to the time-dependent Kohn–Sham equation [22]. Here, $\mathcal{H}_{\text{mixed}}^{\text{QP}}(\mathbf{r}; \mathbf{R}(t))$ denotes the QP (*GW*) Hamiltonian for the mixed state constructed by these wavepackets [24]. We introduce the QP wavefunctions $\varphi_n^{\text{QP}}(\mathbf{r}; \mathbf{R}(t))$ and the QP energies $\varepsilon_n^{\text{QP}}(\mathbf{R}(t))$ [$n = i$ (occupied) or a (unoccupied), QP level indices], which satisfy the eigenvalue equation

$$\mathcal{H}_{\text{mixed}}^{\text{QP}}(\mathbf{r}; \mathbf{R}(t)) \varphi_n^{\text{QP}}(\mathbf{r}; \mathbf{R}(t)) = \varepsilon_n^{\text{QP}}(\mathbf{R}(t)) \varphi_n^{\text{QP}}(\mathbf{r}; \mathbf{R}(t)) \quad (3)$$

during the simulation. Then, using the spectral method [24,29,33], we can expand the wavepackets $\phi_\lambda(\mathbf{r}; \mathbf{R}(t), t)$ as

$$\phi_\lambda(\mathbf{r}; \mathbf{R}(t), t) = \sum_n \varphi_n^{\text{QP}}(\mathbf{r}; \mathbf{R}(t)) c_{n\lambda}(t) \quad (4)$$

with the expansion coefficients

$$c_{n\lambda}(t) = \langle \varphi_n^{\text{QP}}(\mathbf{R}(t)) | \phi_\lambda(\mathbf{R}(t), t) \rangle. \quad (5)$$

The TDQP Equation (2) can be numerically solved by propagating the wavepackets in small timesteps Δt . The wavepackets $\phi_\lambda(\mathbf{r}; \mathbf{R}(t + \Delta t), t + \Delta t)$ at a slightly later time $t + \Delta t$ with a small time interval Δt can be expressed as

$$\begin{aligned} \phi_\lambda(\mathbf{r}; \mathbf{R}(t + \Delta t), t + \Delta t) &= \exp \left[-i \int_t^{t+\Delta t} \mathcal{H}_{\text{mixed}}^{\text{QP}}(\mathbf{r}; \mathbf{R}(t)) dt \right] \phi_\lambda(\mathbf{r}; \mathbf{R}(t), t) \\ &\approx \sum_n \exp \left[-i \varepsilon_n^{\text{QP}}(\mathbf{R}(t + \Delta t)) \right] \varphi_n^{\text{QP}}(\mathbf{r}; \mathbf{R}(t + \Delta t)) c_{n\lambda}(t + \Delta t) \end{aligned} \quad (6)$$

with

$$\begin{aligned} c_{n\lambda}(t + \Delta t) &= \langle \varphi_n^{\text{QP}}(\mathbf{R}(t + \Delta t)) | \phi_\lambda(\mathbf{R}(t), t) \rangle \\ &\approx \langle \varphi_n^{\text{QP}}(\mathbf{R}(t)) | \phi_\lambda(\mathbf{R}(t), t) \rangle + \Delta t \frac{\partial}{\partial t'} \langle \varphi_n^{\text{QP}}(\mathbf{R}(t')) | \phi_\lambda(\mathbf{R}(t), t) \rangle_{t'=t} \\ &= c_{n\lambda}(t) - \Delta t \sum_m c_{m\lambda}(t) \sum_I \dot{\mathbf{R}}_I(t) \langle \varphi_n^{\text{QP}}(\mathbf{R}(t)) | \nabla_{\mathbf{R}_I} | \varphi_m^{\text{QP}}(\mathbf{R}(t)) \rangle. \end{aligned} \quad (7)$$

In the last equality of Equation (7), we used Equation (4) again. The second term of the rightmost expression in Equation (7) is proportional to the nuclear velocity $\dot{\mathbf{R}}_I(t) = d\mathbf{R}_I(t)/dt$ and represents a non-adiabatic interaction [34,35]. The matrix elements $\mathbf{d}_{nm} = \langle \varphi_n^{\text{QP}}(\mathbf{R}(t)) | \nabla_{\mathbf{R}_I} | \varphi_m^{\text{QP}}(\mathbf{R}(t)) \rangle$ represent the non-adiabatic coupling vectors.

2.2. One-Shot GW Within TDQP

We apply this formalism to the one-shot GW approach [36], which is the simplest and most reliable approach in the GWA. In the one-shot GW approach, the QP wavefunctions are replaced by Kohn–Sham orbitals in the local density approximation (LDA) [36]

$$\varphi_n^{\text{QP}}(\mathbf{r}; \mathbf{R}(t)) \approx \varphi_n^{\text{LDA}}(\mathbf{r}; \mathbf{R}(t)), \quad (8)$$

and the QP energy eigenvalues $\varphi_n^{\text{QP}}(\mathbf{r}; \mathbf{R}(t))$ are calculated from the LDA eigenvalues $\varphi_n^{\text{LDA}}(\mathbf{r}; \mathbf{R}(t))$ and the exchange-correlation potential $\mu_{\text{xc}}^{\text{LDA}}(\mathbf{r})$ as

$$\varepsilon_n^{\text{QP}}(\mathbf{R}(t)) \approx \varepsilon_n^{\text{LDA}}(\mathbf{R}(t)) + \langle \varphi_n^{\text{LDA}}(\mathbf{R}(t)) | [\Sigma_{\text{xc}}(\varepsilon_n^{\text{QP}}(\mathbf{R}(t))) - \mu_{\text{xc}}^{\text{LDA}}] | \varphi_n^{\text{LDA}}(\mathbf{R}(t)) \rangle, \quad (9)$$

where $\Sigma_{\text{xc}}(\varepsilon_n^{\text{QP}}(\mathbf{R}(t)))$ is the exchange-correlation part of the self-energy, which does not include the Hartree term. The self-energy $\Sigma_{\text{xc}}(\varepsilon_n^{\text{QP}}(\mathbf{R}(t)))$ in Equation (9) explicitly depends on the resulting QP energy $\varepsilon_n^{\text{QP}}(\mathbf{R}(t))$. The QP energy obtained in a previous time step can be used as the argument for self-energy in the present time step. Therefore, the renormalization procedure using the Z factor [36] is not required in the present time-dependent approach. The usage of the QP energies $\varepsilon_n^{\text{QP}}(\mathbf{R}(t))$, which are obtained by Equation (9) in Equation (6), is the distinguishing feature of the TDGW approach. Except for this difference, everything else remains the same as in the TDDFT dynamics formulation. The Newtonian equation of motion for NA-ES-TDGW-MD is approximated as

$$\begin{aligned} M_I \frac{d^2 \mathbf{R}_I(t)}{dt^2} &= -\nabla_{\mathbf{R}_I} E_{\text{ref}}^{(N)}(\mathbf{R}(t), t) \\ &\approx -\nabla_{\mathbf{R}_I} E_{\text{LDA}}^{(N)}(\mathbf{R}(t), t), \end{aligned} \quad (10)$$

where $E_{\text{ref}}^{(N)}(\mathbf{R}(t), t)$ and $E_{\text{LDA}}^{(N)}(\mathbf{R}(t), t)$ denote the GW total energy and the approximate LDA total energy, respectively, of an N -electron reference state. Although the exchange-correlation contribution to the total energy is approximated by its LDA form, the wavepackets used for TD charge densities are updated by Equation (6). Therefore, $E_{\text{LDA}}^{(N)}(\mathbf{R}(t), t)$ is not the typical LDA total energy, but it includes the QP effects via the QP Hamiltonian $\mathcal{H}_{\text{mixed}}^{\text{QP}}(\mathbf{r}; \mathbf{R}(t))$.

2.3. Ab Initio Cloning in NA-ES-TDGW-MD

In our approach, the nuclear trajectory evolves as the gradient of the average potential generated by the electrons, which is a mean-field approximation in the Ehrenfest framework. In this mean-field approximation, the correlation (also known as quantum coherence) between the electron “motion” and nuclear trajectory is neglected. This suffers from the problem of strong non-adiabatic mixing particularly when two Born–Oppenheimer (BO) surfaces cross or approach each other. A proper description of such correlations requires a

distinct classical trajectory for each electronic state, which is provided by an SH strategy, such as that proposed by Tully [37,38] or Makhov et al. [35]. In this work, we adopt the SH strategy proposed by Makhov et al. [35] named *ab initio* (multiple) cloning in our dynamics formalism, although our approach does not include multiple trajectory basis functions.

A quantity that is used as a measure of quantum (de)coherence, i.e., hopping from a mixed surface (with index λ) to a pure BO surface (with index n) is called the “breaking force” $\mathbf{F}_{\lambda \rightarrow n}^{\text{br}}$. The indices λ and n typically indicate the newly occupied/empty QP level (OCC1/EMP1; see Section 3.1) in the QP representation. The breaking force is defined as

$$\mathbf{F}_{\lambda \rightarrow n}^{\text{br}} = (1 - |c_{n\lambda}(t)|^2) \Delta \mathbf{F}_{n\lambda}(t), \quad (11)$$

where $c_{n\lambda}(t)$ are the coefficients in the expansion of the wavepacket as defined in Equation (5) or (7) and $\Delta \mathbf{F}_{n\lambda}(t)$ is the deviation of the force felt by the nuclei on a pure BO surface ($-\nabla_{\mathbf{R}_I} E_n^{(N)}(\mathbf{R}(t), t)$) from the mean-field force in Equation (10) ($\nabla_{\mathbf{R}_I} E_\lambda^{(N)}(\mathbf{R}(t), t)$):

$$\Delta \mathbf{F}_{n\lambda}(t) = \nabla_{\mathbf{R}_I} E_\lambda^{(N)}(\mathbf{R}(t), t) - \nabla_{\mathbf{R}_I} E_n^{(N)}(\mathbf{R}(t), t). \quad (12)$$

The condition for a hop (or “clone” in Ref. [35]) is that the breaking acceleration $a_{\lambda \rightarrow n}^{\text{br}}$ is greater than a pre-decided threshold δ_{clone}

$$a_{\lambda \rightarrow n}^{\text{br}} = |\mathbf{M}^{-1} \mathbf{F}_{\lambda \rightarrow n}^{\text{br}}| > \delta_{\text{clone}}. \quad (13)$$

In this work, we define $\delta_{\text{clone}} = 3 \times 10^{-6}$ a.u. for exploring the surface hop time as in our previous study [24].

2.4. Computational Details

Since the eigenstates span the complete Hilbert space, we use the all-electron mixed-basis approach [24,29,33,39,40] implemented in our home-grown *ab initio* package named Tohoku mixed basis orbitals (TOMBO) [41], in which the one-electron orbitals are expressed by both plane waves (PWs) and atomic orbitals (AOs). We use a simple cubic unit cell of 12 Å, where the Coulomb interaction is spherically cut to avoid interactions with adjacent unit cells. The 14147 PWs corresponding to the 17.3 Ry cutoff energy and minimal number of numerical AOs have finite values only within each non-overlapping atomic sphere. AOs are smoothly truncated by subtracting a smooth quadratic function, which has the same amplitude and derivative at the atomic sphere surface [41]. This quadratic function smoothly connecting to the tail of the true orbital can be successfully described by a linear combination of PWs. The cutoff energies corresponding to 69 Ry and 7.7 Ry are set, respectively, for the exchange and correlation parts of the self-energy. 190 levels are used in the spectral decomposition [24] and in the calculation of the correlation part of the self-energy. The generalized plasmon pole model [36] is used to avoid frequency integration. We performed tests to ensure that all these parameters are sufficient for obtaining good convergence of results. However, we increased the cutoff energies to 44 Ry (for PWs), 111 Ry (for exchange), and 11 Ry (for correlation) as well as the number of levels to 3500 when a separate one-shot GW calculation was performed.

The precursor to performing a TDGW molecular dynamics simulation is to obtain converged electronic states at a given electron configuration within the LDA. Once convergence is achieved, the dynamics simulation is performed by updating the wavepackets stepwise in $\Delta t = 0.01$ fs intervals, where the Hamiltonian is expected to change very slightly. The wavepackets are the same as the QP (Kohn–Sham) eigenfunctions for the ES reference at $t = 0$. We perform 20 sub-loops of electronic state updates after every update of the atomic positions, to ensure that the total energy is conserved. The GW calculation is performed only during the final 20th sub-loop, and the QP energies and atomic positions are updated subsequently.

3. Results

The initial geometry of the $\text{CH}_4 + \text{Ni}$ system is shown in the leftmost panel in Figure 1. The Ni atom is placed at a C–Ni bond distance of 2.00 Å, which is the stable distance for carbon chemisorption on a Ni(111) surface [42]. Two H atoms (H1 and H2) are away from the Ni atom while the other two (H3 and H4) face the Ni atom. We impose symmetry breaking of the initial geometry of CH_4 by slightly elongating one of the C–H bonds facing the Ni atom (H4) by 0.05 Å. The $\text{CH}_4 + \text{Ni}$ system has a triplet ground state with 20 α -spin (\uparrow -spin) and 18 β -spin (\downarrow -spin) electrons. The charge density distribution of each QP level for the GS reference of this geometry is depicted in Figure 1. Here, and hereafter, the charge density implies the absolute value of the QP wavefunction-squared irrespective of its occupancy.

From a single-shot GW calculation for the GS reference, the QP energies are obtained as presented in Table 1. Since the 14th level, which corresponds to the HOMO of the methane fragment (indicated by ‘*’ in Table 1), is slightly shallower for β -spin than that for α -spin, we chose the β -spin for electron excitations to the LUMO. The QP energies of the 14th $\text{HOMO}-4_\beta$ (HOMO of CH_4), 13th $\text{HOMO}-5_\beta$ (HOMO-1 of CH_4), and LUMO_β levels are, respectively, $\varepsilon_{\text{HOMO}-4_\beta} = -14.9$ eV, $\varepsilon_{\text{HOMO}-5_\beta} = -15.1$ eV, and $\varepsilon_{\text{LUMO}_\beta} = -1.0$ eV. Therefore, the ionization potential (IP) of the methane fragment at the GS of the $\text{CH}_4 + \text{Ni}$ system, i.e., the energy required to remove one electron from the 14th $\text{HOMO}-4_\beta$ level, is $-\varepsilon_{\text{HOMO}-4_\beta} = 14.9$ eV which is higher than that of pristine methane (GW: 13.7 ± 0.5 eV [24] and experiments: 12.6–14.8 eV [43–45]), while the electron affinity (EA) of the $\text{CH}_4 + \text{Ni}$ system at the GS, i.e., the energy obtained by adding one electron to the 19th LUMO_β level, is $-\varepsilon_{\text{LUMO}_\beta} = 1.0$ eV. The higher IP and positive EA values in $\text{CH}_4 + \text{Ni}$ are attributed to the presence of the Ni d orbitals.

The slightly distorted CH_4 still has a nearly two-fold degenerate HOMO_β (13th and 14th β -spin levels of the $\text{CH}_4 + \text{Ni}$ system), whose QP wavefunctions exhibit two different orientations with respect to the Ni atom, see Figure 1d,e. Therefore, the trajectory differs depending on which level is excited. Here, we show two significantly different trajectories when an electron is excited from the 13th/14th β -spin level to the 19th empty (LUMO) level. The 13th→19th level excitation involves the movement of the two H atoms facing Ni (H3 and H4 in Figure 1) while the 14th→19th level excitation involves the movement of the two H atoms away from Ni (H1 and H2 in Figure 1). We first present the latter case before presenting the former.

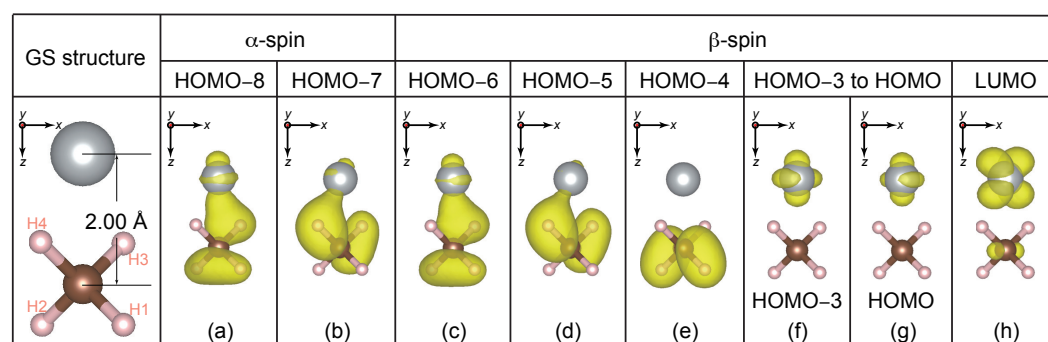


Figure 1. Initial geometry (leftmost panel) and (a–h) charge densities of the relevant α - and β -spin QP levels for the GS reference. The isosurface for the charge density plots was set at 1×10^{-8} electrons/Å³. The directions of viewing are indicated for reference.

Table 1. The calculated QP energies (in units of eV) within the GWA for the GS reference using the initial geometry. The 14th level (14*) corresponds to the CH₄ HOMO.

Level	α -Spin (eV)		β -Spin (eV)	
21	LUMO	−1.0	LUMO+2	−0.3
20	HOMO	−6.9	LUMO+1	−0.8
19	HOMO−1	−9.9	LUMO	−1.0
18	HOMO−2	−10.3	HOMO	−8.9
17	HOMO−3	−10.4	HOMO−1	−9.5
16	HOMO−4	−10.6	HOMO−2	−9.3
15	HOMO−5	−10.6	HOMO−3	−9.4
14*	HOMO−6	−15.0	HOMO−4	−14.9
13	HOMO−7	−15.7	HOMO−5	−15.1
12	HOMO−8	−16.0	HOMO−6	−15.8
11	HOMO−9	−23.8	HOMO−7	−23.6

3.1. H Ejection Opposite to the Ni Side

In this case, we excite an electron from the slightly shallower HOMO _{β} level of CH₄, which is the 14th HOMO−4 _{β} level of the CH₄ + Ni system, to the empty Ni 3d level, which is the 19th LUMO _{β} level. Now, the original HOMO−4 _{β} is called “EMP1 _{β} ” and the original LUMO _{β} , “OCC1 _{β} ”. The labels such as OCC# _{α/β} and EMP# _{α/β} with # = 1, 2, ... indicate the lower occupied and higher empty levels, respectively. This nomenclature is based on the level ordering at $t = 0$ and will be constantly used even if the order of the levels changes during the simulation.

The time evolution of the QP energy eigenvalues $\varepsilon_n^{\text{QP}}(\mathbf{R}(t))$ of the α - and β -spin levels is shown, respectively, in Figure 2a,b, while, the charge densities of the different levels of interest are shown at $t = 3.8, 10.8, 25.8,$ and 32.6 fs in a tabular format below the QP energy plots in Figure 3.

The levels of interest are (a) OCC9 (GS 12th HOMO−8 level), (b) OCC8 (GS 13th HOMO−7 level), (c) OCC7 (GS 14th HOMO−6 level) for α -spin, and (d) OCC7 (GS 12th HOMO−6 level), (e) OCC6 (GS 13th HOMO−5 level), (f) EMP1 (GS 14th HOMO−4 level), (g) OCC5 (GS 15th HOMO−3 level), (h) OCC2 (GS 18th HOMO level), (i) OCC1 (GS 19th LUMO level) for β -spin. The alphabets a-i followed by the simulation time in femtoseconds (fs) are used to represent the charge density panels.

At $t = 0$, the QP energies of the β -spin OCC1 and EMP1 levels are, respectively, $\varepsilon_{\text{OCC1}\beta} = -6.7$ eV [thick orange dotted line in Figure 2b] and $\varepsilon_{\text{EMP1}\beta} = -9.6$ eV [thick violet dashed-dotted-dashed line in Figure 2b]. They are the Ni 3d orbital and the CH₄ bonding orbital as seen in Figure 1h,e, respectively. According to EQPT, $\varepsilon_{\text{HOMO-4}\beta} = E_{\text{GS}} - E_{\text{HOMO-4}\beta}$ and $\varepsilon_{\text{OCC1}\beta} = E_{\text{photo}} - E_{\text{HOMO-4}\beta}$, where E_{GS} , E_{photo} , and $E_{\text{HOMO-4}\beta}$ are the total energies of the GS, the photoexcited state, and the $(N - 1)$ -electron state with one electron missing at the the 14th HOMO−4 _{β} level, respectively. Note that $\varepsilon_{\text{HOMO-4}\beta}$ is equal to $-\text{IP}$ of the methane fragment in the CH₄ + Ni system. Similarly, $\text{EA} = E_{\text{GS}} - E_{\text{anion}}$ and $\varepsilon_{\text{EMP1}\beta} = E_{\text{anion}} - E_{\text{photo}}$, where E_{anion} is the total energy of the anionic state with one electron added to the LUMO level of the GS. From these relations, the photoabsorption energy (PAE) for this excitation $E_{\text{photo}} - E_{\text{GS}}$ can be obtained in two different ways, $\varepsilon_{\text{OCC1}\beta} - \varepsilon_{\text{HOMO-4}\beta} = -6.7 - (-14.9)$ eV = 8.2 eV and $-\text{EA} - \varepsilon_{\text{EMP1}\beta} = -1.0 - (-9.6)$ eV = 8.6 eV. The similarity in these two values clearly indicates the accuracy of our calculation. The resulting PAE (the averaged value is 8.4 eV) is about 1.8 eV lower than that for pristine CH₄ (10.2 eV [5–7]).

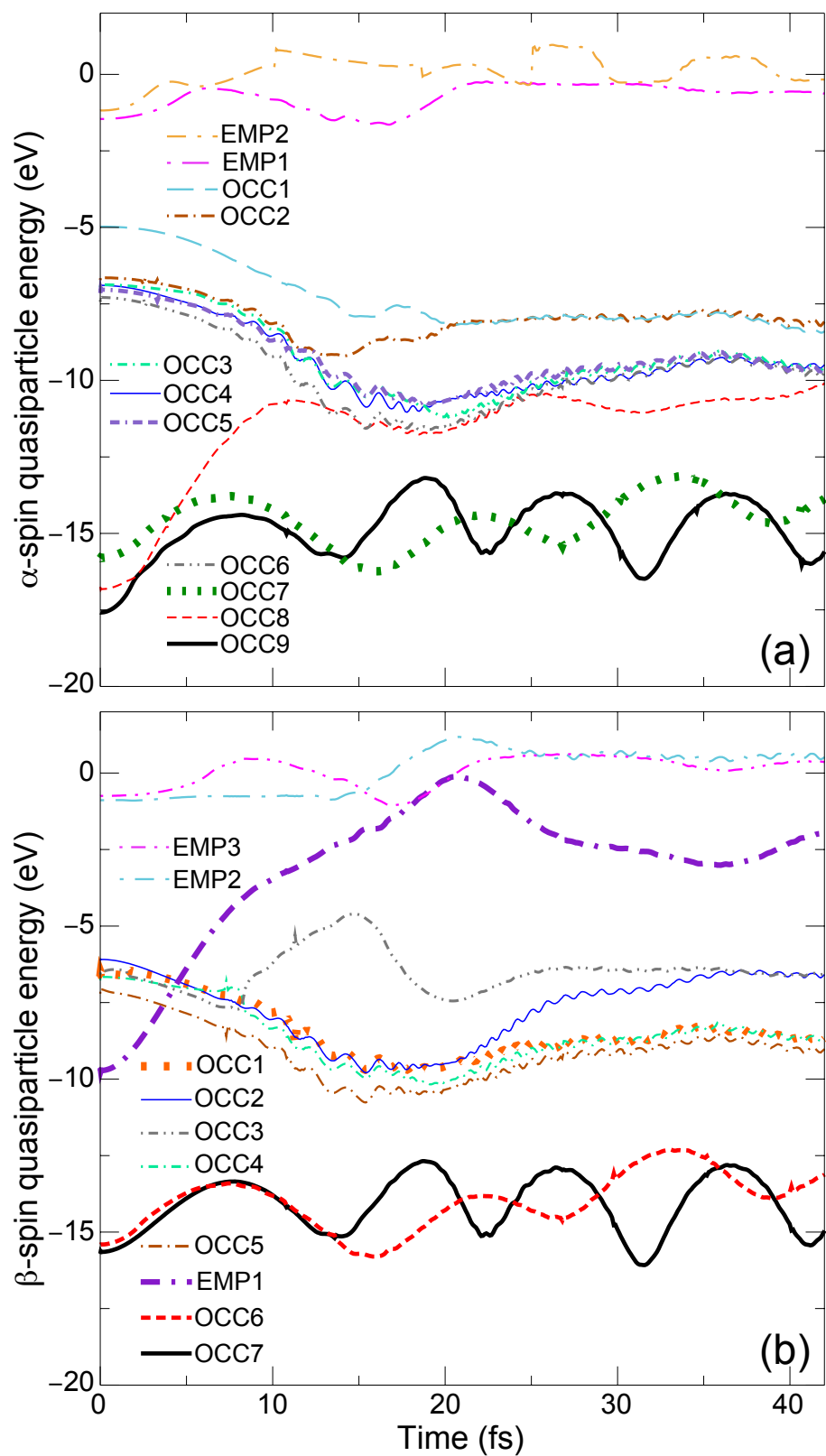


Figure 2. Time evolution of (a) α -spin and (b) β -spin QP energy eigenvalues $\epsilon_n^{\text{QP}}(\mathbf{R}(t))$.

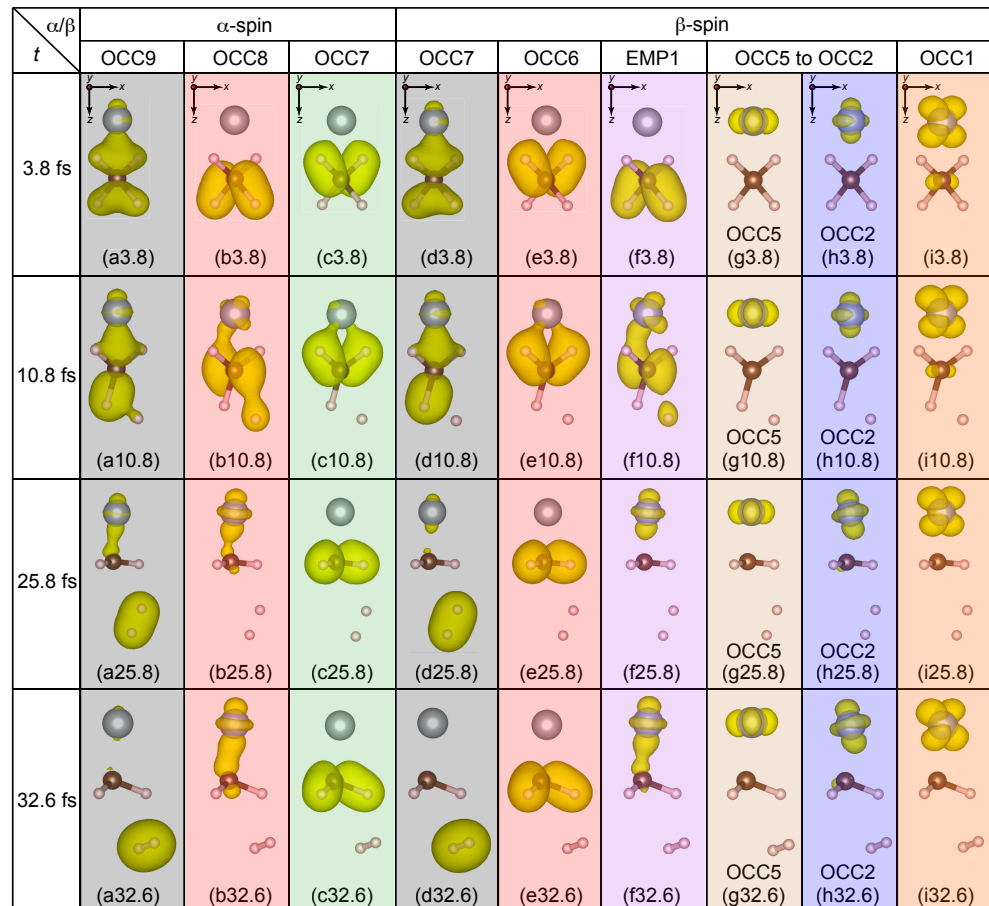


Figure 3. Panels (a–i) represent the charge densities of the levels of interest for the H ejection opposite to the Ni side for each time instant at $t = 3.8, 10.8, 25.8,$ and 32.6 fs. The isosurface for the charge density plots was set at 1×10^{-8} electrons/ \AA^3 . The directions of viewing are indicated for reference in the uppermost panels (a).

At $t = 3.8$ fs, we see that the charge densities of all QP levels [Figure 3a–i3.8] do not change significantly from those of the GS [Figure 1a–h], with the exception that the OCC8_α and OCC7_α levels for the ES reference [Figure 3b,c3.8] are the swapped $\text{HOMO}-7_\alpha$ [Figure 1b] and $\text{HOMO}-6_\alpha$ (not shown in Figure 1) levels for the GS reference. On the other hand for $4 \leq t < 5$ fs, the EMP1_β level [thick violet dashed-dotted-dashed line in Figure 2b] crosses with the other OCC5_β – OCC1_β levels [OCC5 – brown dotted-dashed line, OCC4, light-green dotted-dashed line, OCC3, gray dotted-dashed-dotted line, OCC2, thin blue solid line, and OCC1, thick orange dotted line in Figure 2b]. The charge density of EMP1_β at $t = 3.8$ fs [Figure 3f3.8] is localized on the methane fragment but its population is shifted to the Ni side at $t = 10.8$ fs [Figure 3f10.8]. On the other hand, the charge density of OCC1 at $t = 3.8$ and 10.8 fs [Figure 3i3.8,10.8] does not change and continues to exhibit a Ni $3d$ character. Therefore, the electronic structure (mainly composed of the occupied orbitals) does not deviate significantly from the BO surface during level crossings, and the breaking acceleration does not exceed the SH threshold value δ_{clone} . Consequently, the simulation is continued without SH. As the simulation progresses, two H atoms opposite the Ni side (H1 and H2 in Figure 1) begin to dissociate from the CH_4 fragment of the $\text{CH}_4 + \text{Ni}$ system.

Interesting parallels emerge in both the α - and β -spin QP energies in Figure 2a,b, respectively. While the QP energies of the OCC8_α [red dashed line in Figure 2a] and the EMP1_β [thick violet dashed-dotted-dashed line in Figure 2b] levels increase (~ -17 eV to ~ -10 eV for OCC8_α and -9.6 eV to ~ -2 eV for EMP1_β) with time, the QP energies of the OCC7_α [thick green dotted line in Figure 2a] and OCC6_β [thick red dashed line in Figure 2b] levels oscillate analogously around ~ -15 eV. The resemblances in the

temporal evolution of OCC9 $_{\alpha}$ and OCC7 $_{\beta}$, OCC8 $_{\alpha}$ and EMP1 $_{\beta}$, and OCC7 $_{\alpha}$ and OCC6 $_{\beta}$ indicate that these orbitals are spin-paired with each other. This is further reflected in the similarities in the charge densities in Figure 3a3.8–32.6,d3.8–32.6 for OCC9 $_{\alpha}$ and OCC7 $_{\beta}$, Figure 3b3.8–32.6,f3.8–32.6 for OCC8 $_{\alpha}$ and EMP1 $_{\beta}$, and Figure 3c3.8–32.6,e3.8–32.6 for OCC7 $_{\alpha}$ and OCC6 $_{\beta}$ throughout the entire duration ($t = 3.8, 10.8, 25.8, \text{ and } 32.6$ fs) of the simulation.

The charge population in both OCC9 $_{\alpha}$ and OCC7 $_{\beta}$ is initially spread toward the Ni side (charge densities for $t = 3.8, 10.8$ fs) before being shifted towards the two ejected H atoms (H1 and H2) at $t = 25.8$ fs [Figure 3a,d25.8]. Subsequently, the H1 and H2 atoms approach each other and begin to form a H–H bond. Finally, at $t = 32.6$ fs, these α - and β -spin levels become the completely isolated σ orbital of H–H [Figure 3a,d32.6]. At this time, the H1–H2 bond length is 0.72 Å, which is very close to the experimental H₂ bond length, 0.74 Å [46], and the bond distances of C–H1 and C–H2 are 2.51 Å and 2.78 Å, respectively, which are both considerably large. We additionally perform a contour analysis of the charge densities shown in Figure 3a,d32.6 to obtain quantitative estimates of charge populations around the H₂ fragment [Supplementary Information Figure S1a]. We compare this with the charge contour of an isolated H₂ molecule obtained from a single-point LDA calculation [Supplementary Information Figure S1b]. We find an extremely good agreement between the TDGW-MD and the LDA results demonstrating the computational reliability of our predicted dynamics using TDGW-MD. Moreover, the QP energies of the OCC9 $_{\alpha}$ and OCC7 $_{\beta}$ levels at $t = 32.6$ fs in Figure 2a,b are, respectively, -15.8 eV and -15.3 eV, which are also very close to the $-IP$ of the hydrogen molecule 15.4 eV [47]. Therefore, we conclude that an isolated hydrogen molecule H₂ is created as a product of this photolysis reaction in this very short time period. Based on this trajectory, we speculate that the photolysis reaction would be $\text{CH}_4 + \text{Ni} \xrightarrow{\hbar\omega=8.4\text{ eV}} \text{CH}_2\text{-Ni} + \text{H}_2$.

3.2. H Ejection Towards the Ni Side

We excite an electron from the slightly deeper HOMO–1 $_{\beta}$ level of CH₄, which is the 13th HOMO–5 $_{\beta}$ level of the CH₄ + Ni system, to the 19th empty Ni 3d LUMO $_{\beta}$ level. The original HOMO–5 $_{\beta}$ is now empty and is called “EMP1 $_{\beta}$ ”, while the original LUMO $_{\beta}$ is now occupied and is called “OCC1 $_{\beta}$ ”. Figure 4a,b shows the early time behavior of the QP energy eigenvalues $\epsilon_n^{\text{QP}}(\mathbf{R}(t))$ of the α - and β -spin levels, respectively. The TDGW and the BO charge densities for the ES reference at $t = 1.7$ fs and $t = 3.7$ fs are shown in Figure 5.

At $t = 0$, the QP energy of EMP1 $_{\beta}$ [violet dashed-dotted-dashed line in Figure 4b] is $\epsilon_{\text{EMP1}_{\beta}} = -9.8$ eV and the QP energy of OCC1 $_{\beta}$ [red dashed line in Figure 4b] is $\epsilon_{\text{OCC1}_{\beta}} = -6.9$ eV. They are the CH₄ bonding orbital and the Ni 3d orbital as seen in the charge density plots in Figure 5a5,7 at $t = 1.7$ fs. From EQPT, the required energy for this photoexcitation can be calculated as either the difference between $\epsilon_{\text{OCC1}_{\beta}}$ of this photoexcited state and $\epsilon_{\text{HOMO-5}_{\beta}}$ of the GS, or the difference between $\epsilon_{\text{LUMO}_{\beta}}$ of the GS state, i.e., $-EA$, and $\epsilon_{\text{EMP1}_{\beta}}$ of this photoexcited state. The former is $-6.9 - (-15.1)$ eV = 8.2 eV and the latter is $-1.0 - (-9.8)$ eV = 8.8 eV, which are close to each other. This again demonstrates the accuracy of our simulation. The resulting PAE (the averaged value is 8.5 eV) is about 1.7 eV lower than that for pristine CH₄ (10.2 eV [5–7]).

At $t = 1.7$ fs, the TDGW and BO charge densities are quite similar to each other as seen in Figure 5a1–7,b1–7. They also resemble the GS charge densities in Figure 1a–h. This indicates that the non-adiabatic effect is very weak at this time. Indeed, the breaking acceleration $a_{\lambda \rightarrow n}^{\text{br}} = 6.13 \times 10^{-10}$ a.u. is much smaller than the threshold value $\delta_{\text{clone}} = 3 \times 10^{-6}$ a.u. In the $2.5 \leq t \leq 3.0$ fs time interval, we see level crossings between the EMP1 $_{\beta}$ level [violet dashed-dotted-dashed line in Figure 4b] and the other OCC5 $_{\beta}$ -OCC1 $_{\beta}$ levels [OCC5, brown dotted-dashed line, OCC4, orange dotted-dashed line, OCC3, gray dotted-dashed-dotted line, OCC2, blue dashed line, and OCC1, red dashed line in Figure 4b]. In contrast, there is no such level crossing in the lower α -spin levels besides that between the EMP1 [pink dashed line in Figure 4a] and EMP2 [light blue dotted-dashed line in Figure 4a] levels at $t = 2.6$ fs.

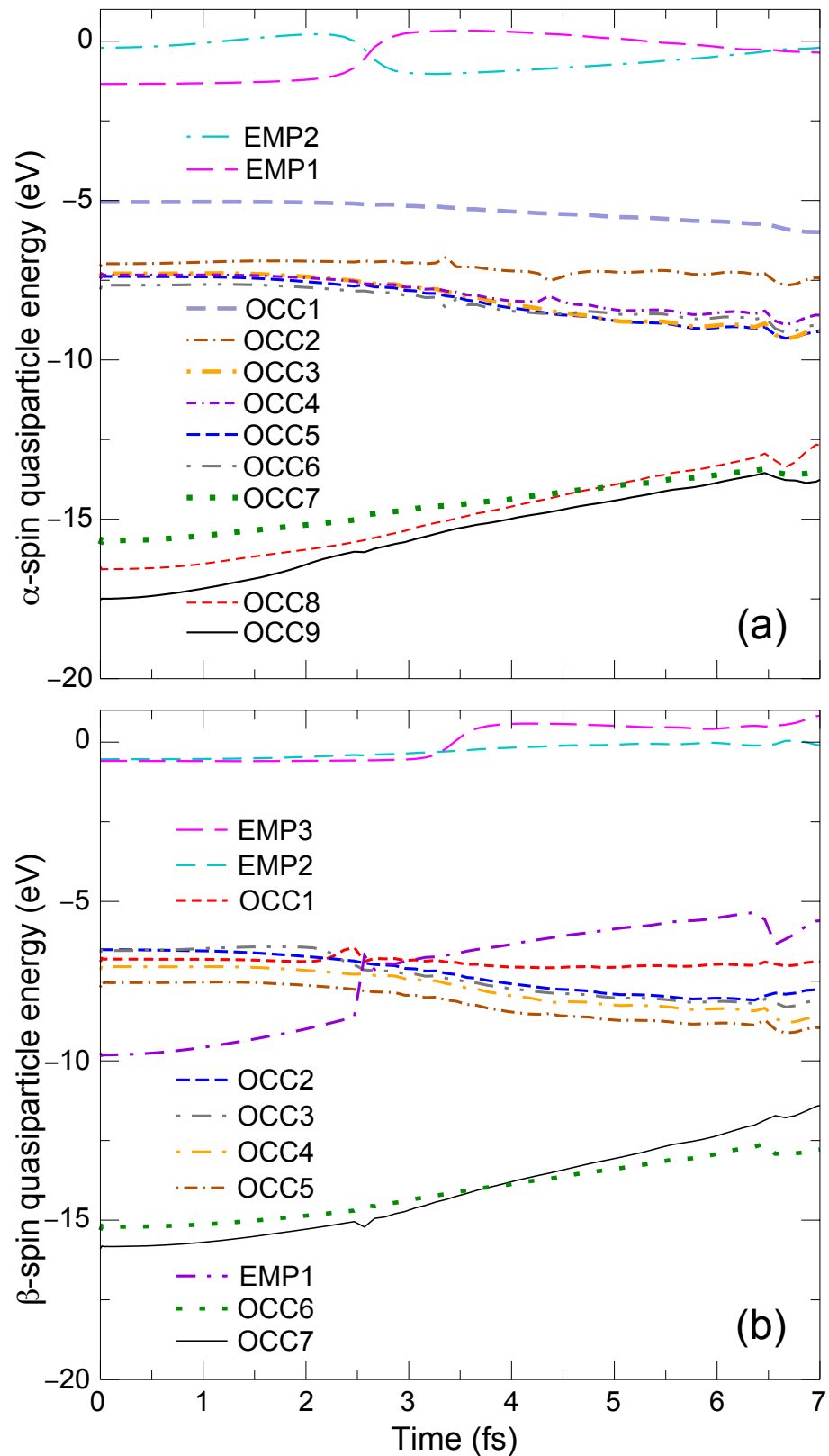


Figure 4. Early time behavior of (a) α -spin, (b) β -spin QP energy eigenvalues $\varepsilon_n^{\text{QP}}(\mathbf{R}(t))$ for the H ejection towards the Ni side.

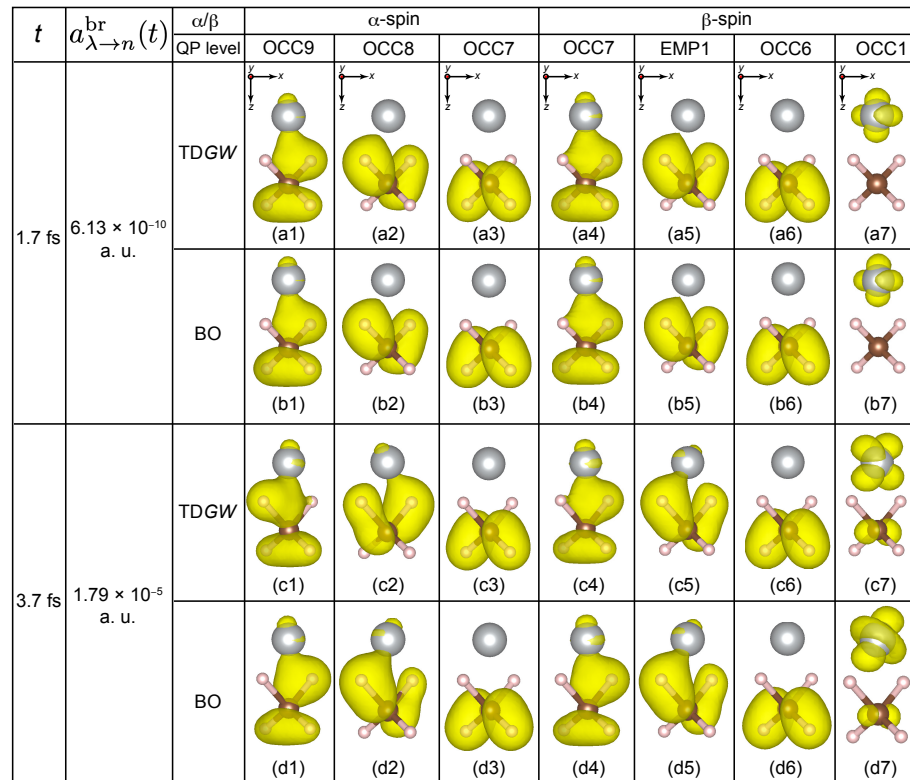


Figure 5. Comparison of TDGW charge densities (**a,c**) with BO charge densities (**b,d**) for the ES reference at $t = 1.7$ fs (a1–7) and (b1–7) and $t = 3.7$ fs (c1–7) and (d1–7). The isosurface for the charge density plots was set at 1×10^{-8} electrons/ \AA^3 . The directions of viewing are indicated for reference in the uppermost panels (**a**).

At $t = 3.7$ fs, the breaking acceleration $a_{\lambda \rightarrow n}^{\text{br}} = 1.79 \times 10^{-5}$ a.u. exceeds the threshold value $\delta_{\text{clone}} = 3 \times 10^{-6}$ a.u., similar to the case of pristine methane [24]. Indeed, the TDGW charge densities at this time instant [Figure 5c1–7] are somewhat different from the BO charge densities with the same geometry [Figure 5d1–7]. For example, those of the OCC9_α and OCC8_α levels are different as if the left and right charge lobes were reversed. Moreover, those of the OCC1_β level are slightly different in terms of the Ni 3d character. Therefore, the simulation undergoes SH at $t = 3.7$ fs. In our Ehrenfest framework, we perform SH to the BO surface for the GS reference.

The time evolution of the QP energies (for the simulation with SH at $t = 3.7$ fs) are shown in Figure 6a,b, respectively, for α - and β -spins while the trajectory of this simulation is presented in Figure 7.

At the SH time, EMP1_β level [violet dashed-dotted-dashed line in Figure 6b] jumps up above the vacuum level, while OCC1_β level [red dashed line in Figure 6b] falls down to ~ -14 eV. Around this SH time, the two H atoms in the Ni side (H3 and H4 in Figure 1) start to move away from the C atom and approach the Ni atom. Thereafter, OCC9_α - OCC7_α , OCC7_β , OCC6_β and OCC1_β levels oscillate in their corresponding QP energies around -14 eV [Figure 6a,b]. The similarity in their temporal variation is reflected in the charge densities shown in Figure 7a–e,g, implying that these orbitals are spin-paired with each other.

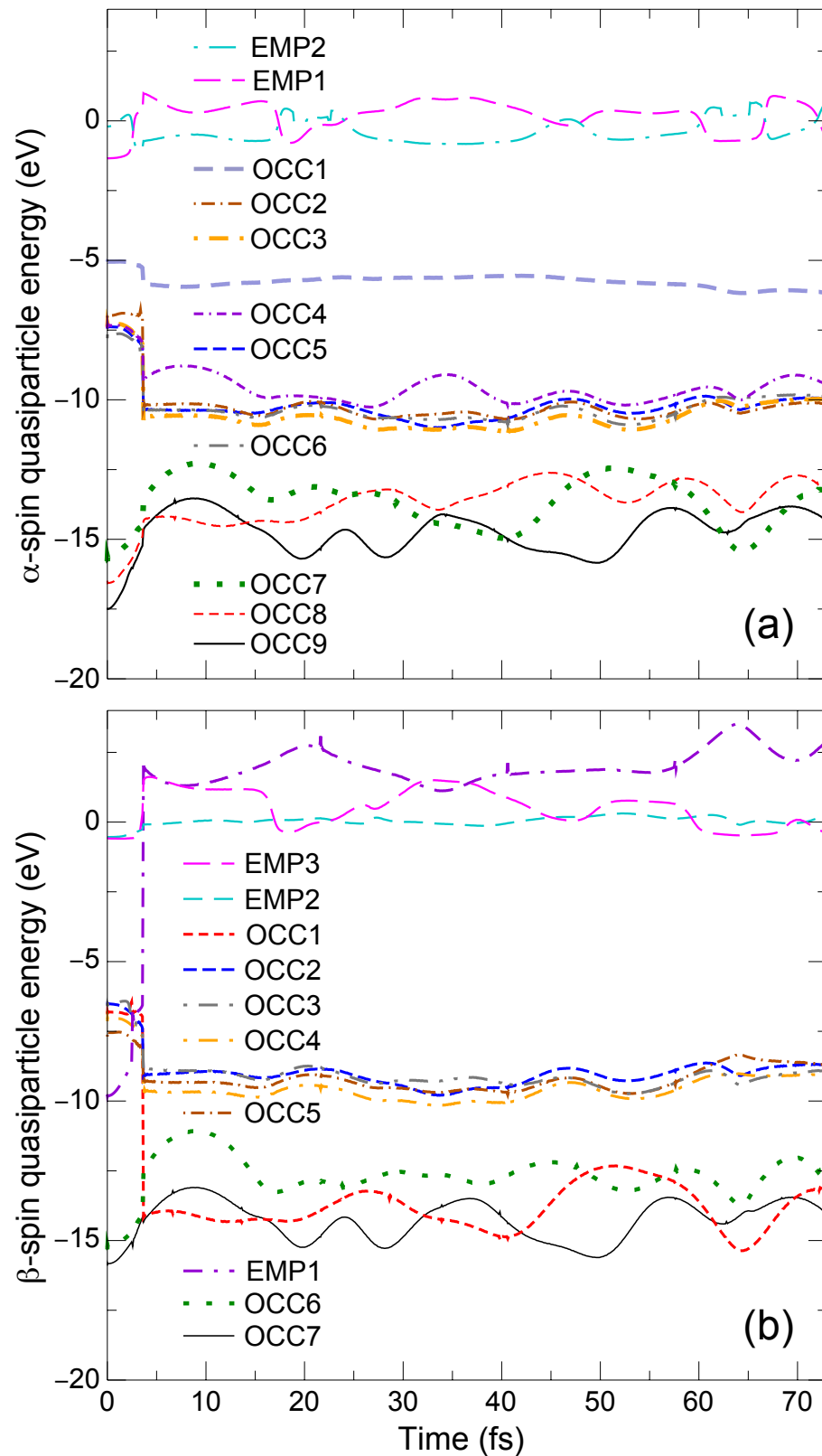


Figure 6. Time evolution of (a) α -spin, (b) β -spin QP energy eigenvalues $\epsilon_n^{\text{QP}}(\mathbf{R}(t))$.

With time, the H3 and H4 atoms begin to move away from the Ni atom. At $t = 22.2$ fs, H3 and H4 return to the methane side, but around the [40.6, 57.6] fs time interval, H3 is bound to the Ni atom. However, this bonding is not strong with the H3–Ni bond being broken, and a subsequent return of H3 toward methane. Finally, at $t = 72.6$ fs, the original geometry is

virtually retrieved. Indeed, the charge densities at $t = 72.6$ shown in Figure 7a–g are very close to those of the GS charge densities in Figure 1. At the same time, interestingly, the Ni atom starts to move away from the CH_4 fragment which is clearly evident at $t = 72.6$ fs from the C–Ni distance around 2.29 \AA . From Figure 6a,b around $t = 72.6$ fs, we see that the QP energies $\varepsilon_{\text{OCC}9_\alpha} - \varepsilon_{\text{OCC}7_\alpha}$, $\varepsilon_{\text{OCC}7_\beta}$, $\varepsilon_{\text{OCC}6_\beta}$, and $\varepsilon_{\text{OCC}1_\beta}$ oscillate in their QP energies around the mean value of -14 eV , which is very close to $-\text{IP} = -13.7 \pm 0.5 \text{ eV}$ of the pristine methane [24]. (Experimental IP is $12.6\text{--}14.8 \text{ eV}$ [43–45].) In addition, all empty levels (EMP1, EMP2, etc.) are above the vacuum level or just close to the vacuum level regardless of the spin, as seen in Figure 6a,b, reflecting the negative EA of the pristine methane molecule. All these observations indicate that the combined $\text{CH}_4\text{--Ni}$ system is undergoing dissociation into the CH_4 and Ni fragments, i.e., $\text{CH}_4 + \text{Ni} \xrightarrow{\hbar\omega=8.5\text{ eV}} \text{CH}_4 + \text{Ni}$.

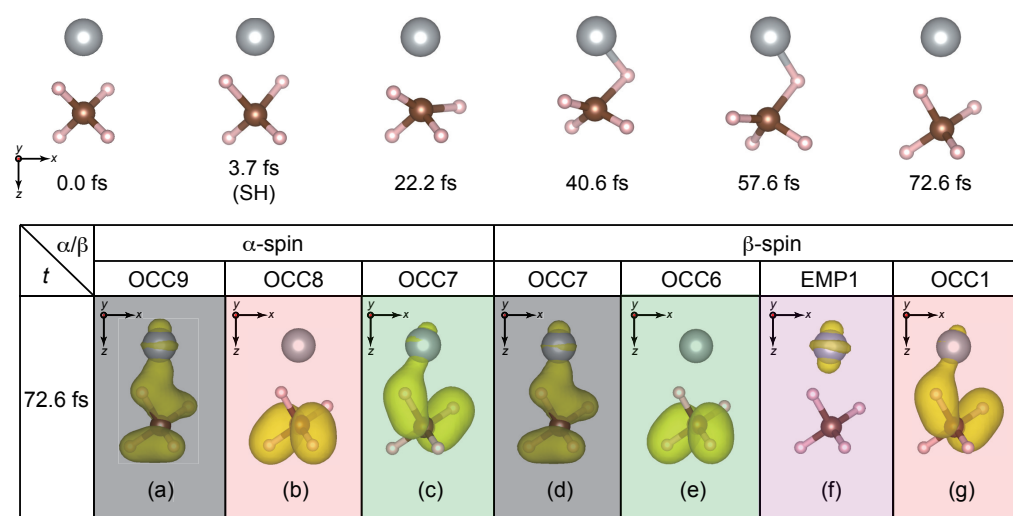


Figure 7. Time evolution of atomic geometry for the H ejection in the Ni side. Panels (a–g) represent charge densities of relevant QP levels at $t = 72.6$ fs. The isosurface for the charge density plots was set at 1×10^{-8} electrons/ \AA^3 . The directions of viewing are indicated for reference.

4. Discussion

We have considered two possible pathways of the photolysis of methane in the presence of a Ni atom depending on either the β -spin 14th ($\text{HOMO-}4_\beta$) level (HOMO of the methane fragment) or the 13th ($\text{HOMO-}5_\beta$) level ($\text{HOMO-}1$ of the methane fragment) being excited to the 19th (LUMO_β) level. In both the cases, we estimated the required PAE in two different ways under EQPT. One approach is $\varepsilon_{\text{OCC}1_\beta}$ of the ES minus $\varepsilon_{\text{HOMO-}4_\beta}$ (or $\varepsilon_{\text{HOMO-}5_\beta}$) of the GS and the other is $-\text{EA}$ minus $\varepsilon_{\text{EMP}1_\beta}$ of the ES. (IP of the methane fragment is $-\varepsilon_{\text{HOMO-}4_\beta}$.) The resulting PAEs via either approach are close to each other, suggesting the accuracy of the present calculation. The PAEs are 8.4 eV and 8.5 eV , respectively, for the 14th and the 13th level excitations which are lower than that of 10.2 eV for pristine methane, indicating the reduction in the PAE due to the existence of a Ni atom. This reduction in PAE is due to the excitation of an electron from a C $2p$ orbital [Figure 1d,e] to an intermediate $3d$ orbital of Ni [Figure 1h] instead of to the higher energy $3s$ orbital of C (in the pristine CH_4 case). As a matter of fact, photolysis of methane on a Pt(111) surface has experimentally been shown to occur at an excitation energy of around 6.4 eV ($\sim 193 \text{ nm}$) [48], which is significantly lower than 10.2 eV ($\sim 122 \text{ nm}$) in the absence of such a substrate further exemplifying the crucial role played by transition metal atoms in making photochemical reactions more accessible.

It is noteworthy that, in both pathways, two hydrogen atoms are simultaneously ejected from the methane molecule at the beginning, which is a distinct characteristic of the present results. On the contrary, in the pristine methane case, only one H atom is ejected by a single photon absorption. Why are two H atoms ejected simultaneously from CH_4 despite undergoing an excitation via a single photon absorption in the presence of a Ni

atom? The reason for this is that the C–H bonds in the CH₄ molecule become considerably weakened while the C–Ni bonding becomes stronger via *p-d* orbital hybridization.

When an electron is excited from the 14th level to the 19th level, two H atoms opposite Ni are ejected from the methane molecule, and they eventually combine to become an isolated hydrogen molecule. The QP energy of the HOMO level of this ejected hydrogen molecule is ~ -15.5 eV irrespective of the spin, which is close to the $-IP$ of the isolated hydrogen molecule 15.4 eV [47]. The QP wavefunction corresponding to the ejected hydrogen molecule is completely localized at the hydrogen molecule, and there is no charge fraction remaining in the CH₂–Ni side (see also Supplementary Information (SI) for the contour plots of the charge density). Thus, we can conclude that a hydrogen molecule is produced as a product. This is a sensational result because two hydrogen atoms are ejected from one methane molecule by a single photon absorption and they automatically combine to become a hydrogen molecule. This clearly demonstrates the important role played by Ni in providing a more efficient route for photolysis. This pathway leads to the formation of the H₂ molecule as there does not exist an ‘absorber’ such as Ni to impede the motion of the two H atoms. This reaction is closely related to the thermocatalytic or solar-aided decomposition of methane, where a transition metal atom or cluster mediates the growth of nanocarbon materials together with the production of hydrogen molecules. For example, there is a possibility that, if two methane molecules are attached to a Ni cluster, the remaining C atoms can combine to produce the C₂ dimer subsequent to several photolysis reactions that may result in the dissociation of four hydrogen molecules. With the addition of more methane molecules, this process may be continued to produce carbon nanomaterials.

In contrast, when two hydrogen atoms facing the Ni atom are ejected, the ejected H atoms cannot escape because of the strong attractive forces exerted by both the Ni and methylene (CH₂) fragments. The two H atoms initially approach the Ni atom due to the inertia of motion but eventually return to the CH₄ fragment. There are three competing factors that govern the entire dynamic: the inertia of motion of the ejected H, the Coulombic interaction between the H and Ni atoms, and the covalent interaction between the H and C atoms. During the initial stage of the photolysis, as the ejected H atoms approach the Ni atom, their inertia of motion carries them away from the C atom; see Figure 7. After SH to the GS-BO surface, the strength of the covalent interaction exceeds this inertia and forces the ejected H atoms to return. With this return, the inertia of motion in the reverse direction increases leading to the H atoms overshooting their original positions at $t = 22.2$ fs. In this process, the overall CH₄ geometry strongly deviates from its stable configuration, which initiates the rebound of one of the H atoms toward Ni. Mediated by a weak Coulomb interaction as a result of charge transfer from this H atom to the Ni atom, this H temporarily bonds with Ni around $t = 40.6$ – 57.6 fs. However, the influence of the C atom continues to persist, leading to the return of this ejected H to the original position at $t = 72.6$ fs [Figure 7a–g]. Because of these three competing factors, none of the H atoms can get dissociated after ejection, but rather prefer to return to (nearly) recover the original methane geometry. At the same time, during the reversal of the H atom from Ni towards CH₄, the increase in the inertia of H in the opposite direction initiates the concerted motion of CH₄ away from Ni. This can be seen not only from the atomic trajectory but also from the fact that methane-derived QP levels have energy values similar to $-IP$ of pristine methane. Therefore, in this case, we conclude that the combined CH₄–Ni system is dissociated into CH₄ and Ni.

We next comment on the reliability of our simulation results despite the short MD simulation times. Photolysis reactions are generally ultrafast [49] as they usually complete within several tens of femtoseconds. Therefore, even though the simulation times seem to be short in our work, the match between QP energies and experimental values for both the trajectories is clearly evident. Therefore, we argue that the present results are reliable.

In addition to the reliability and accuracy of our results, these were obtained in reasonable wall clock times. The simulation of H ejection away from/toward Ni took 6/10 days using four nodes with 48 MPI processes on the Numerical Materials Simulator supercomputer at the National Institute for Materials Science.

Through our simulations, we show how two H atoms can be dissociated via a single photon absorption eventually leading to the formation of an isolated H₂ molecule. This is achieved at a much lower PAE of 8.4 eV, compared to pristine methane (10.2 eV). Overall, our work presents an opportunity for experimental verification of our observations. The results obtained from our simulations are accurate as they are obtained without any adjustable/fitting parameters and are based on sound mathematical principles.

Supplementary Materials: The following supporting information can be downloaded at: <https://www.mdpi.com/article/10.3390/nano14221775/s1>, Figure S1: Contour plots of the H₂ charge density; MD Trajectory S1: away_from_Ni_MD.xyz; MD Trajectory S2: towards_Ni_MD.xyz; see Data Availability Statement to view these .xyz files.

Author Contributions: Conceptualization, K.O., R.S. and Y.K.; methodology, A.M. and K.O.; software, A.M., K.O., R.S. and Y.K.; validation, A.M., K.O., R.S. and Y.K.; investigation, A.M.; resources, R.S.; writing—original draft preparation, A.M. and K.O.; writing—review and editing, R.S. and Y.K.; visualization, A.M.; supervision, R.S.; project administration, R.S.; funding acquisition, R.S., Y.K. and K.O. All authors have read and agreed to the published version of the manuscript.

Funding: This research was funded by the Japan Society for the Promotion of Science (JSPS) KAKENHI grant numbers 21H01607, 21H01877, 23K21094 and 24K01149, and by Asian Office of Aerospace Research and Development (AOARD) grant number FA2386-22-1-4024.

Data Availability Statement: The data that support the findings of this study are available within the article and its supplementary files, away_from_Ni_MD.xyz and towards_Ni_MD.xyz. The xyz files can be visualized using the VMD software package [50]. The TOMBO executable used for performing NA-ES-TDGW-MD simulations and one-shot GW calculations is available upon request.

Acknowledgments: The calculations in this study were performed using the Numerical Materials Simulator at the National Institute for Materials Science (NIMS); System B at the Institute for Solid State Physics (ISSP), the University of Tokyo, the MASAMUNE supercomputing system at the Center for Computational Materials Science, Institute for Materials Research (IMR), Tohoku University (Proposal Nos. 202308-SCKGE-0216, 202312-SCKXX-0206 and 202311-SCKXX-0501) and the JHPCN system project (Project IDs: jh220037 and jh230038). Y.K. was supported by (i) the National Science, Research, and Innovation Fund (NSRF) (NRIIS Project No. 90465); (ii) Thailand Science Research and Innovation (TSRI) and (iii) Suranaree University of Technology (SUT).

Conflicts of Interest: The authors declare no conflicts of interest.

Abbreviations

The following abbreviations are used in this manuscript:

DFT	density functional theory
TD	time-dependent
TDDFT	time-dependent density functional theory
LDA	local density approximation
ALDA	adiabatic local density approximation
MD	molecular dynamics
ES	excited state
GS	ground state
QP	quasiparticle
EQPT	extended quasiparticle theory
vac	vacuum level
GWA	GW approximation
SH	surface hopping
TDGW	Non-adiabatic excited-state time-dependent GW
PW	plane wave
AO	atomic orbital
HOMO	highest occupied molecular orbital
LUMO	lowest unoccupied molecular orbital
IP	ionization potential

EA	electron affinity
PAE	photoabsorption energy

References

1. Mokhatab, S.; Mak, J.Y.; Valappil, J.V.; Wood, D.A. *Handbook of Liquefied Natural Gas*, 3rd ed.; Gulf Professional Publishing: Boston, MA, USA, 2014; pp. 1–624.
2. Gunaseelan, V.N. Anaerobic digestion of biomass for methane production: A review. *Biomass Bioenergy* **1997**, *13*, 83–114. [[CrossRef](#)]
3. Züttel, A. Hydrogen storage methods. *Naturwissenschaften* **2004**, *91*, 157–172. [[CrossRef](#)] [[PubMed](#)]
4. Yousefi, M.; Donne, S. Experimental study for thermal methane cracking reaction to generate very pure hydrogen in small or medium scales by using regenerative reactor. *Front. Energy Res.* **2022**, *10*, 1. [[CrossRef](#)]
5. Laufer, A.H.; McNesby, J.R. Photolysis of methane at 1236-Å: Quantum yield of hydrogen formation. *J. Chem. Phys.* **1968**, *49*, 2272–2278. [[CrossRef](#)]
6. Rebbert, R.; Ausloos, P. Photolysis of methane: Quantum yield of C(¹D) and CH. *J. Photochem.* **1972**, *1*, 171–176. [[CrossRef](#)]
7. Brownsword, R.; Hillenkamp, M.; Laurent, T.; Vatsa, R.; Volpp, H.-R.; Wolfrum, J. Quantum yield for H atom formation in the methane dissociation after photoexcitation at the Lyman- α (121.6 nm) wavelength. *Chem. Phys. Lett.* **1997**, *266*, 259–266. [[CrossRef](#)]
8. Lee, L.C.; Chiang, C.C. Fluorescence yield from photodissociation of CH₄ at 1060–1420 Å. *J. Chem. Phys.* **1983**, *78*, 688–691. [[CrossRef](#)]
9. Mebel, A.M.; Lin, S.-H.; Chang, C.-H. Theoretical study of vibronic spectra and photodissociation pathways of methane. *J. Chem. Phys.* **1997**, *106*, 2612–2620. [[CrossRef](#)]
10. York, A.P.; Xiao, T.; Green, M.L. Brief overview of the partial oxidation of methane to synthesis gas. *Top. Catal.* **2003**, *22*, 345–358. [[CrossRef](#)]
11. Matsumura, Y.; Nakamori, T. Steam reforming of methane over nickel catalysts at low reaction temperature. *Appl. Catal. A Gen.* **2004**, *258*, 107–114. [[CrossRef](#)]
12. Ashik, U.P.M.; Daud, W.M.A.W.; Abbas, H.F. Production of greenhouse gas free hydrogen by thermocatalytic decomposition of methane—A review. *Renew. Sust. Energ. Rev.* **2015**, *44*, 221–256. [[CrossRef](#)]
13. Keipi, T.; Tolvanen, H.; Kontinen, J. Economic analysis of hydrogen production by methane thermal decomposition: Comparison to competing technologies. *Energy Convers. Manag.* **2018**, *159*, 264–273. [[CrossRef](#)]
14. Qian, J.X.; Chen, T.W.; Enakonda, L.R.; Liu, D.B.; Basset, J.-M.; Zhou, L. Methane decomposition to pure hydrogen and carbon nano materials: State-of-the-art and future perspectives. *Int. J. Hydrogen Energy* **2020**, *45*, 15721–15743. [[CrossRef](#)]
15. Fan, Z.; Weng, W.; Zhou, J.; Gu, D. Xiao, W. Catalytic decomposition of methane to produce hydrogen: A review. *J. Energy Chem.* **2021**, *58*, 415–430. [[CrossRef](#)]
16. Pham, C.Q.; Siang, T.J.; Kumar, P.S.; Ahmad, Z.; Xiao, L.; Bahari, M.B.; Cao, A.N.T.; Rajamohan, N.; Qazaq, A.S.; Kumar, A.; et al. Production of hydrogen and value-added carbon materials by catalytic methane decomposition: A review. *Environ. Chem. Lett.* **2022**, *20*, 2339–2359. [[CrossRef](#)]
17. Abanades, S.; Kimura, H.; Otsuka, H. Hydrogen production from CO₂-free thermal decomposition of methane: Design and on-sun testing of a tube-type solar thermochemical reactor. *Fuel Process. Tech.* **2014**, *122*, 153–162. [[CrossRef](#)]
18. Pinilla, J.L.; Torres, D.; Lázaro, M.J.; Suelves, I.; Moliner, R.; Cañadas, I.; Rodríguez, J.; Vidal, A.; Martínez, D. Metallic and carbonaceous-based catalysts performance in the solar catalytic decomposition of methane for hydrogen and carbon production. *Int. J. Hydrogen Energy* **2012**, *37*, 9645–9655. [[CrossRef](#)]
19. Boretti, A. A perspective on the production of hydrogen from solar-driven thermal decomposition of methane. *Int. J. Hydrogen Energy* **2021**, *46*, 34509–34514. [[CrossRef](#)]
20. Jia, S.; Cao, X.; Yuan, X.; Yu, K.-T. Multi-objective topology optimization for the solar thermal decomposition of methane reactor enhancement. *Chem. Eng. Sci.* **2021**, *231*, 116265. [[CrossRef](#)]
21. Hohenberg, P.; Kohn, W. Inhomogeneous electron gas. *Phys. Rev.* **1964**, *136*, B864–B871. [[CrossRef](#)]
22. Runge, E.; Gross, E.K.U. Density-functional theory for time-dependent systems. *Phys. Rev. Lett.* **1984**, *52*, 997–1000. [[CrossRef](#)]
23. Petersilka, M.; Gossmann, U.J.; Gross, E.K.U. Excitation energies from time-dependent density-functional theory. *Phys. Rev. Lett.* **1996**, *76*, 1212–1215. [[CrossRef](#)] [[PubMed](#)]
24. Manjanath, A.; Sahara, R.; Ohno, K.; Kawazoe, Y. Non-adiabatic excited-state time-dependent GW molecular dynamics (TDGW) satisfying extended Koopmans’ theorem: An accurate description of methane photolysis. *J. Chem. Phys.* **2024**, *160*, 184102. [[CrossRef](#)] [[PubMed](#)]
25. Ohno, K.; Ono, S.; Isobe, T. A simple derivation of the exact quasiparticle theory and its extension to arbitrary initial excited eigenstates. *J. Chem. Phys.* **2017**, *146*, 084108. [[CrossRef](#)] [[PubMed](#)]
26. Ohno, K.; Esfarjani, K.; Kawazoe, Y. *Computational Materials Science: From Ab Initio to Monte Carlo Methods*, 2nd ed.; Springer: Heidelberg, Germany, 2018; pp. 1–427.
27. Morrell, M.M.; Parr, R.G.; Levy, M. Calculation of ionization potentials from density matrices and natural functions, and the long-range behavior of natural orbitals and electron density. *J. Chem. Phys.* **1975**, *62*, 549–554. [[CrossRef](#)]
28. Smith, D.W.; Day, O.W. Extension of Koopmans’ theorem. I. Derivation. *J. Chem. Phys.* **1975**, *62*, 113–114. [[CrossRef](#)]
29. Sahara, R.; Mizuseki, H.; Sluiter, M.H.F.; Ohno, K.; Kawazoe, Y. Effect of a nickel dimer on the dissociation dynamics of a hydrogen molecule. *RSC Adv.* **2013**, *3*, 12307–12312. [[CrossRef](#)]

30. Burghgraef, H.; Jansen, A.P.J.; van Santen, R.A. Electronic structure calculations and dynamics of methane activation on nickel and cobalt. *J. Chem. Phys.* **1994**, *101*, 11012–11020. [[CrossRef](#)]
31. Sun, Q.; Li, Z.; Du, A.; Chen, J.; Zhu, Z.; Smith, S.C. Theoretical study of two states reactivity of methane activation on iron atom and iron dimer. *Fuel* **2012**, *96*, 291–297. [[CrossRef](#)]
32. Wang, J.-T.; Chen, C.; Ohno, K.; Wang, E.; Chen, X.-L.; Wang, D.-S.; Mizuseki, H.; Kawazoe, Y. Atomistic nucleation and growth mechanism for single-wall carbon nanotubes. on catalytic nanoparticle. *Nanotechnology* **2010**, *21*, 115602. [[CrossRef](#)]
33. Pham, T.N.; Ono, S.; Ohno, K. *Ab initio* molecular dynamics simulation study of successive hydrogenation reactions of carbon monoxide producing methanol. *J. Chem. Phys.* **2016**, *144*, 144309. [[CrossRef](#)] [[PubMed](#)]
34. Saalman, U.; Schmidt, R. Non-adiabatic quantum molecular dynamics: Basic formalism and case study. *Z. Phys. D Atom. Mol. Cl.* **1996**, *38*, 153–163. [[CrossRef](#)]
35. Makhov, D.V.; Glover, W.J.; Martinez, T.J.; Shalashilin, D.V. *Ab initio* multiple cloning algorithm for quantum nonadiabatic molecular dynamics. *J. Chem. Phys.* **2014**, *141*, 054110. [[CrossRef](#)] [[PubMed](#)]
36. Hybertsen, M.S.; Louie, S.G. Electron correlation in semiconductors and insulators: Band gaps and quasiparticle energies. *Phys. Rev. B* **1986**, *34*, 5390–5413. [[CrossRef](#)] [[PubMed](#)]
37. Tully, J.C.; Preston, R.K. Trajectory surface hopping approach to non-adiabatic molecular collisions: The reaction of H⁺ with D₂. *J. Chem. Phys.* **1971**, *55*, 562–572. [[CrossRef](#)]
38. Tully, J.C. Molecular dynamics with electronic transitions. *J. Chem. Phys.* **1990**, *93*, 1061–1071. [[CrossRef](#)]
39. Ohno, K.; Manjanath, A.; Kawazoe, Y.; Hatakeyama, R.; Misaizu, F.; Kwon, E.; Fukumura, H.; Ogasawara, H.; Yamada, Y.; Zhang, C.; et al. Extensive First-Principles Molecular Dynamics Study on the Li Encapsulation into C₆₀ and Its Experimental Confirmation. *Nanoscale* **2018**, *10*, 1825–1836. [[CrossRef](#)]
40. Ohtsuki, T.; Manjanath, A.; Ohno, K.; Inagaki, M.; Sekimoto, S.; Kawazoe, Y. Creation of Mo/Tc@C₆₀ and Au@C₆₀ and molecular-dynamics simulations. *RSC Adv.* **2021**, *11*, 19666–19672. [[CrossRef](#)]
41. Ono, S.; Noguchi, Y.; Sahara, R.; Kawazoe, Y.; Ohno, K. TOMBO: All-electron mixed-basis approach to condensed matter physics. *Comput. Phys. Commun.* **2015**, *189*, 20–30. [[CrossRef](#)]
42. Klinke, D.J.; Wilke, S.; Broadbelt, L.J. A Theoretical Study of Carbon Chemisorption on Ni(111) and Co(0001) Surfaces. *J. Catal.* **1998**, *158*, 540–554. [[CrossRef](#)]
43. Watanabe, K. Ionization potentials of some molecules. *J. Chem. Phys.* **1957**, *26*, 542–547. [[CrossRef](#)]
44. Collin, J.E.; Delwiche, J. Ionization of methane and its electronic energy levels. *Can. J. Chem.* **1967**, *45*, 1875–1882. [[CrossRef](#)]
45. Cook, P.A.; Ashfold, M.N.R.; Jee, Y.-J.; Jung, K.-H.; Harich, S.; Yang, X. Vacuum ultraviolet photochemistry of methane, silane and germane. *Phys. Chem. Chem. Phys.* **2001**, *3*, 1848–1860. [[CrossRef](#)]
46. Huber, K.P.; Herzberg, G. Molecular spectra and molecular structure. In *Constants of Diatomic Molecules*; Van Nostrand Reinhold Co.: New York, NY, USA, 1979; Volume IV.
47. Herzberg, G.; Jungen, C. Rydberg series and ionization potential of the H₂ molecule. *J. Mol. Spectrosc.* **1972**, *41*, 425–486. [[CrossRef](#)]
48. Gruzdkov, Y.A.; Watanabe, K.; Sawabe, K.; Matsumoto, Y. Photochemical C–H bond activation of methane on a Pt(111) surface. *Chem. Phys. Lett.* **1994**, *227*, 243–247. [[CrossRef](#)]
49. Troß, J.; Carter-Fenk, K.; Cole-Filipiak, N.C.; Schrader, P.; Word, M.; McCaslin, L.M.; Head-Gordon, M.; Ramasesha, K. Excited-state dynamics during primary C–I homolysis in acetyl iodide revealed by ultrafast core-level spectroscopy. *J. Phys. Chem. A* **2023**, *127*, 4103–4114. [[CrossRef](#)]
50. Humphrey, W.; Dalke, A.; Schulten, K. VMD: Visual molecular dynamics. *J. Mol. Graph.* **1996**, *14*, 33–38. [[CrossRef](#)]

Disclaimer/Publisher’s Note: The statements, opinions and data contained in all publications are solely those of the individual author(s) and contributor(s) and not of MDPI and/or the editor(s). MDPI and/or the editor(s) disclaim responsibility for any injury to people or property resulting from any ideas, methods, instructions or products referred to in the content.